Materials Today Bio 29 (2024) 101297

Contents lists available at ScienceDirect

Materials Today Bio

journal homepage: www.journals.elsevier.com/materials-today-bio

Injectable hydrogels for Fenton-like Mn^{2+}/Fe^{2+} delivery with enhanced chemodynamic therapy prevent osteosarcoma recurrence and promote wound healing after excision surgery

Lutong Wang [a,1], Haoyu Guo [a,1], Weiyue Zhang [b,1], Xingyin Li [a], Ziliang Su [a], Xin Huang [a,*]

[a] Department of Orthopaedics, Union Hospital, Tongji Medical College, Huazhong University of Science and Technology, Wuhan, 430022, China
[b] Department of Endocrinology, Union Hospital, Tongji Medical College, Huazhong University of Science and Technology, Wuhan, 430022, China

ARTICLE INFO

Keywords:
Recurrent osteosarcoma
Surgical wound healing
Injectable hydrogel
Chemodynamic therapy
Fenton reaction

ABSTRACT

Local recurrence of osteosarcoma and wound healing after excision surgery are major challenges in clinical research. The present anti-tumor treatments could inhibit normal tissues, resulting in difficulties in surgical wound healing. In this study, we constructed an injectable hydrogel as a platform to co-deliver MnO_2 nanoparticles and ferrocene Fc, termed as (MnO_2/Fc)@PLGA for osteosarcoma treatment and wound healing after excision. By simple local injection, the hydrogel could form a protective barrier on the surgical wound after osteosarcoma excision, which could promote wound healing and steady release of MnO_2/Fc nanoparticles. The released MnO_2/Fc might undergo the Fenton reaction through Mn^{2+}/Fe^{2+} to inhibit osteosarcoma cells with chemodynamic therapy (CDT). Furthermore, MnO_2 could catalyze endogenous H_2O_2 to produce O_2, which eliminates the adverse effects of H_2O_2 and remodels the hypoxic state in the local lesions. The increased O_2 facilitated surgical wound healing and anti-tumor effects by regulating the hypoxia inducible factor-1 functions. In conclusion, (MnO_2/Fc)@PLGA hydrogel could effectively prevent local recurrence of osteosarcoma and promote wound healing after excision surgery, thereby providing a novel strategy for tumor treatment and tissue repair.

1. Introduction

Osteosarcoma is the most common primary malignant bone tumor, which mostly affects children and teenagers [1,2]. Currently, the standard treatment of osteosarcoma mainly includes surgery and chemotherapy (including adjuvant chemotherapy and neoadjuvant chemotherapy), and only surgical resection of the tumor can be the final cure [3,4]. However, complete surgical resection of osteosarcoma is very challenging, and residual tumor cells could still survive in the surrounding area, leading to local relapse of osteosarcoma [5]. Therefore, postoperative chemotherapy for osteosarcoma is also crucial for minimizing the relapse or metastasis of osteosarcoma [6,7]. However, the resulting serious toxic and side effects, such as leukopenia (increasing the risk of infection), severe vomiting, nephrotoxicity, ototoxicity, alopecia, and so on, will seriously affect the quality of life of patients [8]. Additionally, these existing methods for osteosarcoma not only kill tumors but also inhibit the formation of healthy tissues, resulting in difficult surgical wound healing. Consequently, novel therapeutic techniques are required to treat osteosarcoma in the clinic, which could lessen the local recurrence of osteosarcoma and promote wound healing after surgery.

Chemodynamic therapy (CDT), a novel ROS-based anti-tumor approach, has generated a lot of concern [9]. With the aid of various catalysts, CDT could transform endogenous hydrogen peroxide (H_2O_2) into the hydroxyl radical (•OH) by a Fenton or Fenton-like reaction to cure tumors [10,11]. CDT does little harm to healthy cells or tissues since it is tumor selective. At present, many anti-tumor properties of CDT resulting from the iron-based Fenton reaction, such as Fe_3O_4 and Fe^{2+}-polyphenol chelates, have now been extensively researched [12,13]. However, the application of iron-based nanoparticles in CDT is constrained by the poor Fenton reaction efficiency in tumor cells [11]. Therefore, the therapeutic effect of CDT can be improved by enhancing the efficiency of the Fenton reaction. It has been demonstrated that the ferrocene (Fc) could decompose the excessive H_2O_2 created by tumor

* Corresponding author.
E-mail address: xin_huang@hust.edu.cn (X. Huang).
[1] Lutong Wang, Haoyu Guo, and Weiyue Zhang contributed equally.

https://doi.org/10.1016/j.mtbio.2024.101297
Received 21 June 2024; Received in revised form 27 September 2024; Accepted 10 October 2024
Available online 11 October 2024

cells due to its redox properties, leading to an increase in ROS in cells, and inducing apoptosis, that is, the Fenton reaction [14,15]. Additionally, the special qualities of Fc, such as non-toxicity, high stability, lipophilicity, and easy functionalization, make it a useful source of ferrous [16,17]. Compared with Fc, Fe_3O_4 nanoparticles are not stable enough, they are more likely to oxidize in air, are unstable in aqueous solutions, have poor water dispersibility, and are prone to aggregation and precipitation [18]. More significantly, Fc derivatives show considerable potential for tumor therapy [19]. Due to the structural diversity, good biosafety, and excellent tumor microenvironment responsiveness, MnO_2 nanoparticles are frequently employed as drug-loaded nanoplatforms and could be highly enriched in the tumor site. Additionally, MnO_2 nanoparticles also might activate H_2O_2/H^+, which can effectively catalyze endogenous H_2O_2 to produce O_2, thus improving the tumor hypoxia microenvironment [20–24]. The resulting Mn^{2+} could also cause a Fenton reaction, enhance CDT, and further promote the tumor killing effect [25–28]. Therefore, MnO_2 nanoparticles loaded with Fc contain two metal ions (Fe^{2+} and Mn^{2+}), which could generate more efficient •OH through Fenton or Fenton-like reaction to achieve effective CDT [29,30].

At present, the local drug delivery system has attracted more and more attention [31–33]. It could cause the drug to accumulate at the desired location, hence enhancing the therapeutic effect and reducing the systemic toxic side effects [34,35]. Injectable and temperature-sensitive hydrogels stand out among them and have been utilized extensively to treat a variety of diseases [36,37]. PLGA-PEG-PLGA is a non-toxic and degradable injectable hydrogel, and when the temperature changes, the hydrogel can transform from a sol state to a gel, which is appropriate for drug loading in vitro and local injection therapy [38–40]. Besides, PLGA hydrogel has outstanding adhesion, mold, and stretching properties that make it a viable choice for covering the wound and accelerating wound healing [41]. Furthermore, angiogenesis contributes to wound healing, while O_2 released from endogenous H_2O_2 decomposition could promote angiogenesis [42–44]. As previously indicated, MnO_2 can efficiently catalyze the synthesis of O_2 from H_2O_2.

Herein, we developed an injectable hydrogel local nanoparticles delivery system. Briefly, MnO_2 nanoparticles and Fc were loaded into

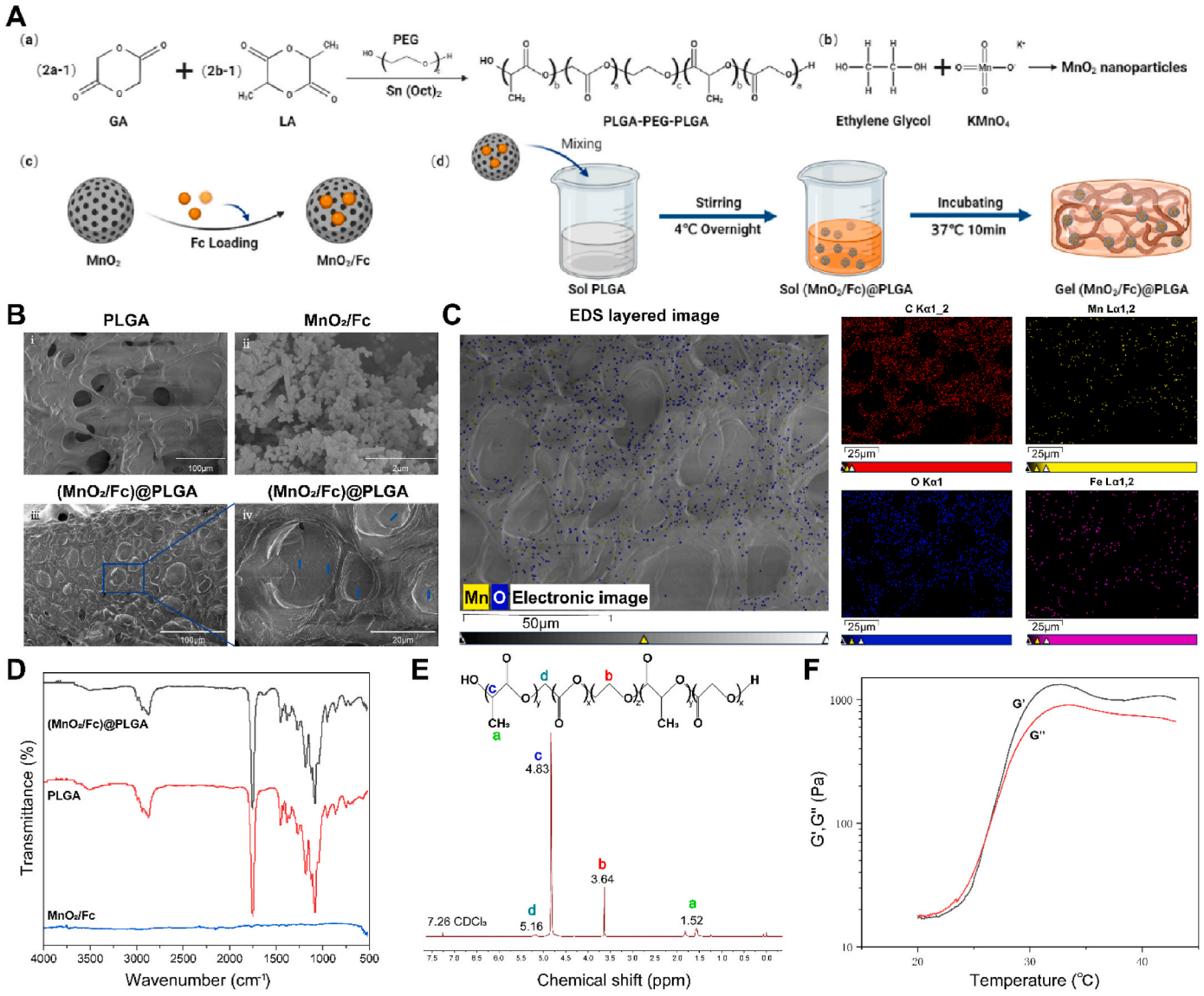

Fig. 1. Preparation and characterization of (MnO_2/Fc)@PLGA hydrogel. (A) Schematic diagram of the preparation of (MnO_2/Fc)@PLGA hydrogel. (B) SEM images of PLGA (i), scale bar: 100 μm, MnO_2/Fc (ii), scale bar: 2 μm, (MnO_2/Fc)@PLGA (iii), scale bar: 100 μm, and the enlarged image of (MnO_2/Fc)@PLGA (iv), scale bar: 20 μm. (C) SEM image and EDS spectrum of C, O, Mn, and Fe of (MnO_2/Fc)@PLGA hydrogel. (D) FTIR spectra of PLGA, MnO_2, and (MnO_2/Fc)@PLGA hydrogel. (E) ^{1}H NMR spectra of PLGA. (F) Rheological behavior of 25 wt% PLGA hydrogel.

the temperature-sensitive hydrogel PLGA-PEG-PLGA to prepare (MnO_2/Fc)@PLGA. After osteosarcoma surgery, (MnO_2/Fc)@PLGA hydrogel was injected into the wound. MnO_2 in the released MnO_2/Fc activated endogenous H_2O_2 to produce O_2 and Mn^{2+}, remodeling the tumor hypoxic microenvironment. The released Fe^{2+} and Mn^{2+} produce •OH through the Fenton and Fenton-like reaction to achieve efficient CDT and inhibit local recurrence of osteosarcoma. The hydrogel could avoid premature nanoparticles leakage. Additionally, the good adhesion and tensile properties of hydrogel could well seal the wound, and the loaded MnO_2 catalyzed H_2O_2 to produce O_2 and facilitate angiogenesis, which together promoted wound healing. In conclusion, (MnO_2/Fc)@PLGA hydrogel could exhibit the promising potential to inhibit local osteosarcoma recurrence and enhance wound healing after surgery.

2. Results and discussions

2.1. Preparation and characterization of (MnO_2/Fc)@PLGA hydrogel

Hydrogels were prepared as shown in Fig. 1A. By ring opening polymerization of lactide (LA) and glycolide (GA) in a molar ratio of 2:1, with PEG acting as an initiator and Sn $(Oct)_2$ acting as a catalyst, PLGA-PEG-PLGA triblock copolymer was created. Take an appropriate amount of synthesized copolymer and sterile double-steamed water to prepare a 25 % aqueous solution to form a temperature-sensitive hydrogel. Additionally, manganese dioxide (MnO_2) nanoparticles were prepared by potassium permanganate ($KMnO_4$) and ethylene glycol. To create the (MnO_2/Fc)@PLGA nanoparticle-loaded hydrogel solution, the produced thermosensitive hydrogel solution was mixed with the necessary quantity of MnO_2 nanoparticles and ferrocene (Fc), stirred at low temperature until well combined, and then left at 4 °C overnight. The (MnO_2/Fc)@PLGA hydrogel was formed by either injecting the solution into animals or incubating the solution at 37 °C.

The microstructure of the hydrogel can be observed by scanning electron microscopy (SEM). The synthesized PLGA-PEG-PLGA hydrogel (PLGA) and (MnO_2/Fc)@PLGA hydrogels both featured a porous network structure (Fig. 1B i and iii). The porous structure of PLGA made it ideal for loading nanoparticles, but it could also facilitate the interchange of oxygen and nutrients, creating an environment that was beneficial for cell growth. Additionally, the morphology of MnO_2/Fc nanoparticles prepared previously was observed by SEM. As shown in Fig. 1B ii, MnO_2/Fc nanoparticles were composed of spherical nanoparticles. Moreover, loading MnO_2/Fc had no discernible impact on the morphology of PLGA, as shown by the SEM image of (MnO_2/Fc)@PLGA (Fig. 1B iii). And in a partially enlarged image of (MnO_2/Fc)@PLGA, MnO_2/Fc nanoparticles (blue arrow) evenly adhered to the hydrogel wall. The energy dispersive X-ray (EDS) spectrum images showed that C, O, Mn and Fe were uniformly distributed on (MnO_2/Fc)@PLGA hydrogel (Fig. 1C). More precisely, Mn and Fe ions was uniformly distributed in the hydrogel. In addition, due to the surface chemistry of MnO_2 and Fc nanoparticles and functional groups, hydrophilic/hydrophobic, resulting in ion adhesion will be different. Fig. 1D showed the Fourier transform infrared spectroscopy (FTIR) of MnO_2/Fc, PLGA, and (MnO_2/Fc)@PLGA. The characteristic absorption peak of PLGA could be seen at 1760 cm^{-1}, which was caused by the stretching vibration of the C=O bond [45]. In MnO_2/Fc, the distinctive Mn-O bond peak was detected at 535 cm^{-1} [46]. These peaks could be observed in the infrared spectrum of (MnO_2/Fc)@PLGA, further demonstrating that loading MnO_2/Fc has no impact on the PLGA structure. In addition, Fig. 1E showed the proton nuclear magnetic resonance (^1H NMR) spectrum of PLGA, thus further confirming its structure. The chemical shift and peak form of PLGA were seen in the ^1H NMR spectrum. Chemical shift peaks for -CH and -CH_3 in LA were about 5.16 ppm and 1.52 ppm, respectively; for -CH_2 in GA, it was approximately 4.83 ppm; and for -CH_2 in PEG, it was approximately 3.64 ppm [47]. These results indicated the successful preparation of (MnO_2/Fc)@PLGA. The rheological analysis results of PLGA were displayed in Fig. 1F. With an increase in temperature, the storage modulus G′ and loss modulus G″ of 25 wt% both rose. Furthermore, G′ rose sharply and intersected with G″ at about 26 °C, indicating that PLGA based hydrogels transitioned from sol state to gel state [45].

2.2. Functions of injectable (MnO_2/Fc)@PLGA hydrogel

As a temperature-sensitive hydrogel, PLGA-PEG-PLGA aqueous solution can be transformed in the sol and gel state. With the increase in temperature, PLGA-PEG-PLGA aqueous solution gradually changed from solution to gel, which is attributed to the formation and aggregation of micelles of hydrophobic PLGA core and hydrophilic PEG shell. The higher the polymer concentration, the lower the sol-to-gel transition temperature, while the higher the gel-to-precipitation transition temperature (Fig. 2A and B). When the polymer concentration increases from 20 wt% to 30 wt%, the sol-to-gel transition temperature decreases from 29 °C to 23 °C. The hydrogel after nanoparticles loading still has temperature-sensitive characteristics, but the sol-to-gel transition of (MnO_2/Fc)@PLGA hydrogel formed after nanoparticles loading is slightly reduced, such as 25 wt% hydrogel (Fig. 2C and D). The sol-gel transition after nanoparticles loading is slightly reduced from 26 °C to 24 °C, which may be due to the hydrogen bond formed between the H atom on ferrocenecarboxylic acid and the PLGA segment in the hydrogel, strengthening the interaction between the hydrophobic bonds of PLGA-PEG-PLGA polymer.

Hydrogels with appropriate injectable and moldable properties could better deliver nanoparticles and thus play a corresponding role. Hydrogels with shear thinning capability can be injected directly into the target area, ensuring complete contact with the tumor or wound. The hydrogels have good injectable and moldable properties before and after MnO_2/Fc loading, and the hydrogels can be molded into different shapes, making them suitable for the treatment of irregularly shaped wounds (Fig. 2E). Furthermore, (MnO_2/Fc)@PLGA hydrogel had good adhesion properties by adhering to the finger well (Fig. 2F) and various material surfaces including glass slide, paper, polypropylene, glass, and polyethylene (Fig. 2G). More importantly, the (MnO_2/Fc)@PLGA hydrogel was also highly adherent to biological tissue, including the heart, liver, spleen, lung, kidney, and skin of mice (Fig. 2H). As a wound dressing, hydrogels may slip off or shatter when applied to a stretchy portion of the body or during physical activities [48]. Therefore, the compressibility and extensibility of hydrogels are critical. The tensile characteristics of (MnO_2/Fc)@PLGA hydrogel were investigated in this study, and the results showed that it could be well compressed and stretched (Fig. 2I). The above results indicated that (MnO_2/Fc)@PLGA hydrogel has good adhesion and extensibility, which can well adhere to and close the wound, prevent poor wound healing caused by stretching, and promote tissue regeneration and wound healing more effectively. Briefly, (MnO_2/Fc)@PLGA hydrogel exhibited good injectability, adhesion, mold, and stretching capabilities, providing greater possibilities for osteosarcoma therapy and wound healing.

The in vitro nanoparticles release behavior and O_2 generation ability of (MnO_2/Fc)@PLGA hydrogel were further investigated. The nanoparticles release curves of MnO_2 and Fc revealed a burst of release in the first two days, followed by a steady slowing and eventual plateau, and the nanoparticles kept releasing for more than 10 days (Fig. 3A). This might be owing to the strong free diffusion of nanoparticles at high concentrations at the beginning, which declined at a certain point and the hydrogel started to degrade and release the nanoparticles. Therefore, the sustained and steady nanoparticles release of (MnO_2/Fc)@PLGA hydrogel might cover the whole anti-tumor and wound healing processes. MnO_2 can react with H_2O_2 to generate O_2, and the presence of H^+ can promote the generation of O_2 from MnO_2 and H_2O_2. To evaluate the O_2 producing capacity of MnO_2 in the tumor microenvironment, we evaluated the quantity of O_2 produced by MnO_2/Fc (Mn, 200 μM) and H_2O_2 solution (100 μM) at various pH (7.4 and 6.5). The rate of O_2 production by MnO_2/Fc at pH 7.4 was slower than at pH 6.5, since the reaction rate of MnO_2 and H_2O_2 will be accelerated at higher H^+

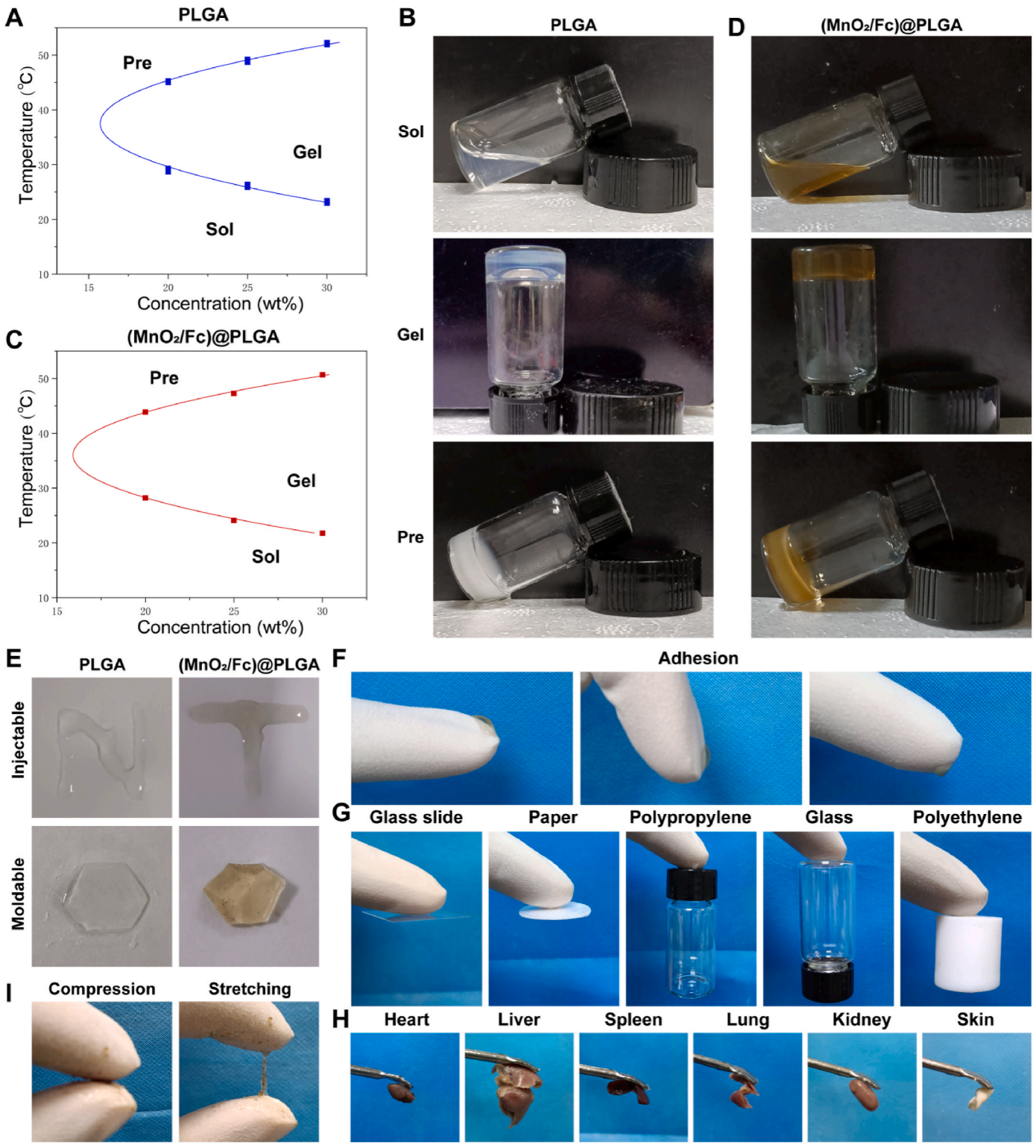

Fig. 2. Functions of injectable (MnO_2/Fc)@PLGA hydrogel. (A, B) Phase diagram and photographs of PLGA. (C, D) Phase diagram and photographs of (MnO_2/Fc)@PLGA. (E) The injectable and moldable of PLGA and (MnO_2/Fc)@PLGA. (F, G, H) Photographs of (MnO_2/Fc)@PLGA adhering to different materials. (I) The compression and stretching of (MnO_2/Fc)@PLGA.

concentration (Fig. 3B).

The degradation and biocompatibility of the hydrogel were then assessed in vitro and in vivo. The hydrogel can be completely degraded after about 40 days in the 37 °C PBS environment (Fig. 3C), demonstrating that it has a sufficient degradation rate. However, it took roughly 21 days for the hydrogel to degrade in vivo. As shown in Fig. 3D, the hydrogel solution could be transformed into gel after 30 min of subcutaneous injection, and then gradually degraded until it was completely degraded on the 21st day. The degradation time in vivo is substantially shorter than that in vitro, most likely due to the complex environment in vivo and the increased contact area with the hydrogel, which accelerated the degradation of the hydrogel. Then the histological

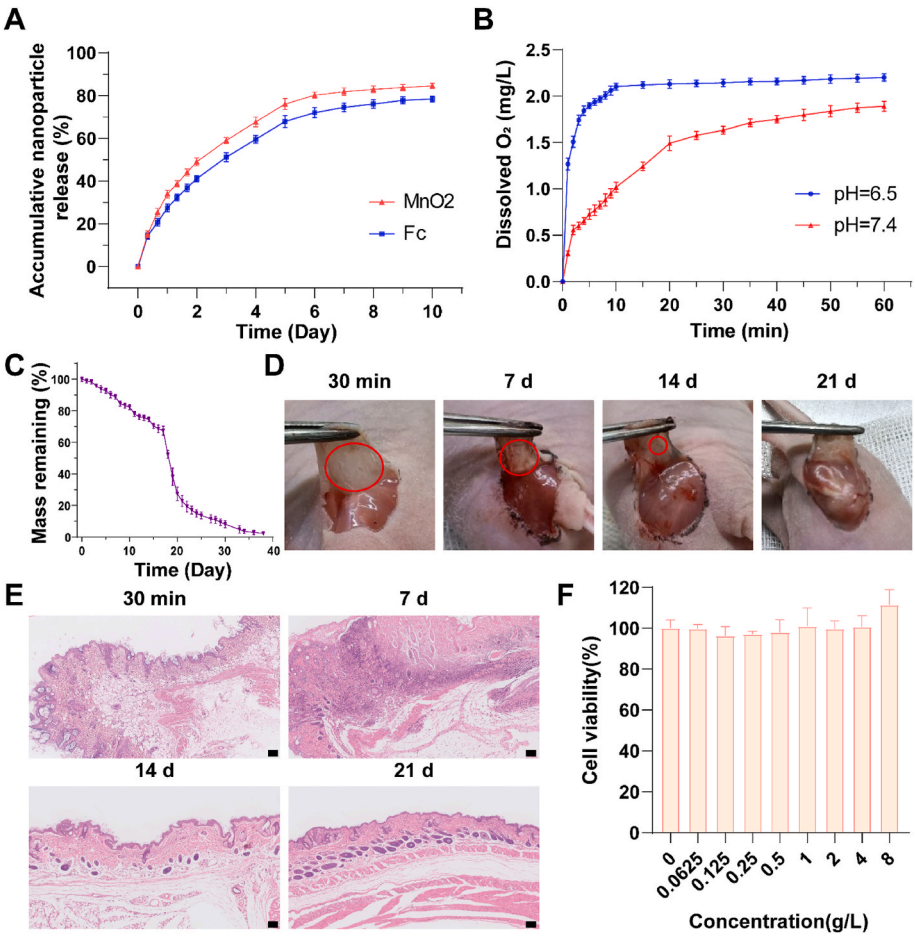

Fig. 3. The nanoparticle release behavior, O_2 generation of (MnO_2/Fc)@PLGA hydrogel, and biocompatibility of PLGA hydrogel. (A) The accumulative release curve of MnO_2 and Fc from (MnO_2/Fc)@PLGA in PBS. (B) O_2 generation at different pH values (6.5 and 7.4) from H_2O_2 solutions (100 μM) with (MnO_2/Fc)@PLGA. (C) The mass remaining of 25 wt% PLGA was incubated in PBS. (D) Photographs of 25 wt% PLGA in vivo after different times (red circl: PLGA). (E) H&E staining of the skin at the injection site of 25 wt% PLGA at different times (scale bar: 100 μm). (F) Cell viability of MNNG/HOS cells treated with PLGA at different concentrations.

changes of the skin at the injection site of the hydrogel were then detected by H&E staining to investigate the histocompatibility of the hydrogel (Fig. 3E). The scattered inflammatory cell infiltration was observed in the skin sections 30 min after hydrogel injection, and after 7 days, there was an increase in inflammatory cells. However, at 14 and 21 days, there was no obvious inflammatory cell infiltration, and the skin basically returned to normal, showing that the body only had a mild inflammatory reaction to the hydrogel and that the hydrogel had good tissue compatibility. Additionally, the cell experiment demonstrated that the viability of the cells was unaffected by the co-culture of hydrogels with cells at concentrations even up to 8 g/L (Fig. 3F). According to the results, hydrogels as implantable materials offer good biocompatibility and degradation, which can reduce the risk of infection and result in little damage to the body.

2.3. *Anti-tumor effects of (MnO_2/Fc)@PLGA hydrogel in vitro*

Based on the successful performance of (MnO_2/Fc)@PLGA hydrogel, the anti-tumor ability of (MnO_2/Fc)@PLGA hydrogel was investigated in vitro. Firstly, the cytotoxicity of (MnO_2/Fc)@PLGA hydrogel was evaluated by CCK-8 analysis, which demonstrated increased cytotoxicity with concentration (Fig. 4A). The survival rate of MNNG/HOS cells was significantly reduced when the concentration was 0.125 g/L, about 80 % of tumor cells were killed. Even at low concentration (0.03125 g/L), (MnO_2/Fc)@PLGA also had a significant killing effect on tumor cells (>50 %). Subsequently, the treatment time of the hydrogel was extended to observe the cell viability of different treatment groups. When the treatment period was extended, the cell viability of the (MnO_2/Fc)@PLGA hydrogel group gradually declined and converged with that of the MnO_2/Fc group (Fig. 4B). At 72 h, the survival rate of (MnO_2/Fc)@PLGA group decreased from 74.33 ± 2.08 % in 24 h to 13.00 ± 2.01 %, which was close to 11.20 ± 1.03 % in MnO_2/Fc group. Live/dead staining was further used to evaluate the apoptosis of tumor cells. The MnO_2/Fc and (MnO_2/Fc)@PLGA hydrogel groups both exhibited intense red fluorescence while exhibiting little green fluorescence, demonstrating that they were both capable of effectively killing tumor cells (Fig. 4C and G). The colony formation assay showed that (MnO_2/Fc)@PLGA hydrogel could significantly suppress the proliferation of tumor cells (Fig. 4D and H). Additionally, the result of the Transwell assay (Fig. 4E and I) demonstrated that treatment with (MnO_2/Fc)@PLGA hydrogel decreased the migration ability of tumor cells. Furthermore, to assess the effect of (MnO_2/Fc)@PLGA on the capacity of tumor cells to produce reactive oxygen species (ROS), DCFH-DA was used for fluorescence images. The MnO_2/Fc and (MnO_2/Fc)@PLGA groups showed strong green fluorescence in contrast to the feeble fluorescence in the control and PLGA groups (Fig. 4F and J). Similar to the results of recent studies, Mn/Fe ions can promote the Fenton-like reaction of H_2O_2 to produce ·OH through co-catalysis [49]. These results indicated that (MnO_2/Fc)@PLGA could boost CDT through the Fenton-like reaction of Mn^{2+} and Fe^{2+}, thus having enhanced anti-tumor ability. However, it was discovered that there were no significant differences between the groups of MnO_2/Fc and (MnO_2/Fc)

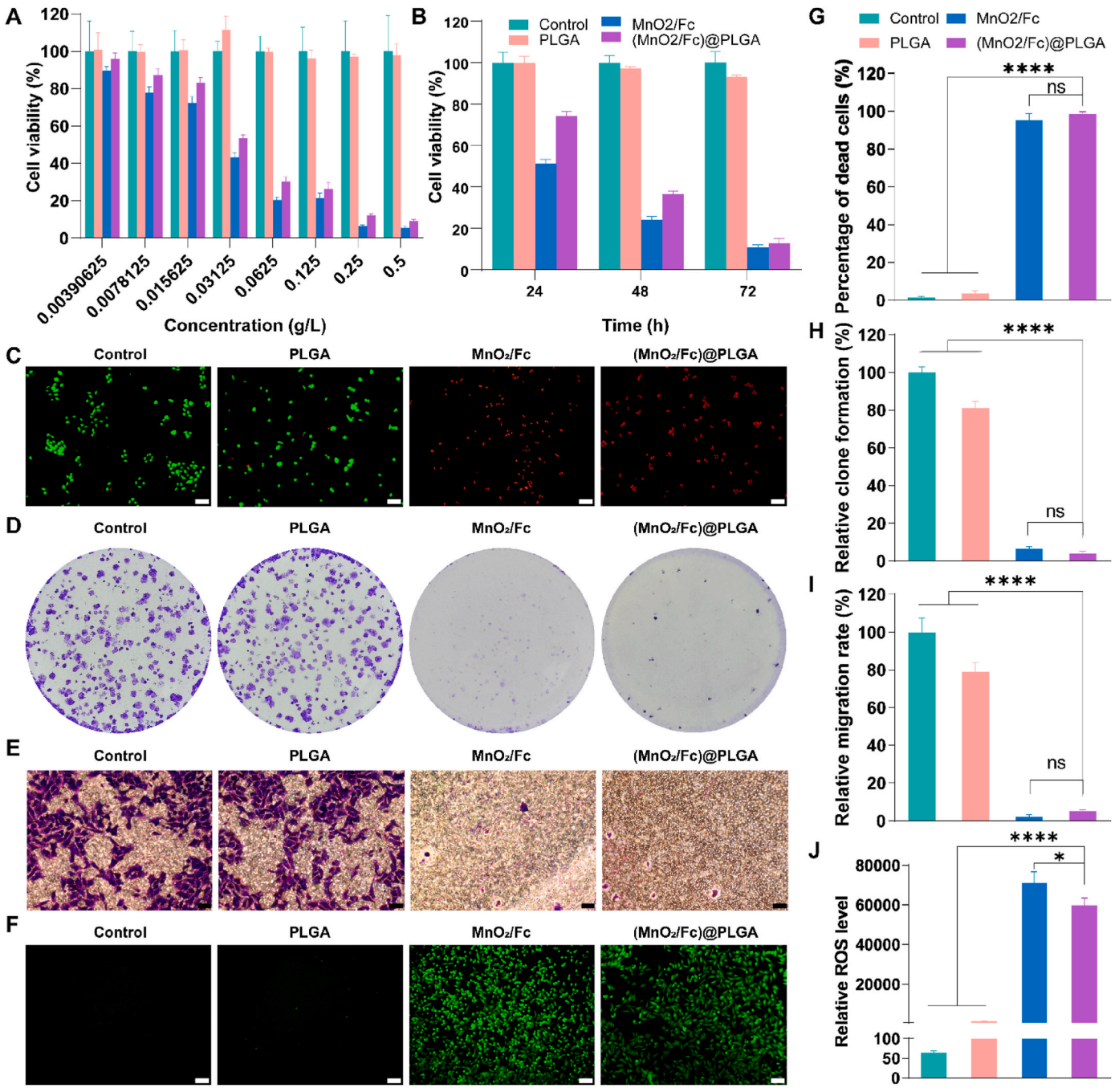

Fig. 4. Anti-tumor effects of (MnO_2/Fc)@PLGA hydrogel in vitro. (A) Cell viability of MNNG/HOS cells treated with various samples at different concentrations. (B) Cell viability of MNNG/HOS cells was treated at different times for each group. (C, G) Live/dead staining of MNNG/HOS cells treated with PLGA, MnO_2/Fc, and (MnO_2/Fc)@PLGA (live cells: green signal, dye with Calcein-AM, dead cells: red signal, dye with PI, scale bar: 100 μm). (D, H) Colony formation assay investigated the effects of PLGA, MnO_2/Fc, and (MnO_2/Fc)@PLGA on the proliferation ability of MNNG/HOS cells (dye with 0.1 % crystal violet). (E, I) Transwell assay exhibited the effect of PLGA, MnO_2/Fc, and (MnO_2/Fc)@PLGA on the migration ability of MNNG/HOS cells (dye with 0.1 % crystal violet, scale bar: 50 μm). (F, J) Fluorescence images and relative ROS level of MNNG/HOS cells treated by PLGA, MnO_2/Fc, and (MnO_2/Fc)@PLGA (tagged with DCFH-DA probe, scale bar: 100 μm, *$p < 0.05$, ****$p < 0.0001$, ns: no significant).

@PLGA in the results of live/dead staining, colony formation and Transwell assays. Even in the DCFH staining experiment, the fluoresced of MnO_2/Fc was stronger than that of the (MnO_2/Fc)@PLGA. This is probably because in vitro cell experiment, MnO_2/Fc directly contacted cells to kill them, whereas (MnO_2/Fc)@PLGA needs to release MnO_2/Fc in order to function as a cell killer. This also indicated that the main function of PLGA is to load MnO_2/Fc.

2.4. Anti-tumor effects of (MnO_2/Fc)@PLGA hydrogel in vivo

We further assessed the anti-tumor effects of (MnO_2/Fc)@PLGA hydrogel in vivo in light of excellent anti-tumor impact in vitro. Balb/c nude mice were subcutaneously injected with MNNG/HOS cells to create the osteosarcoma xenograft model. When the volume of tumors reached about 50 mm^3, different treatments (PBS, PLGA, MnO_2/Fc, and (MnO_2/Fc)@PLGA) were injected around the tumor. Body weight and tumor volume were measured daily for 10 days. As shown in Fig. 5A and

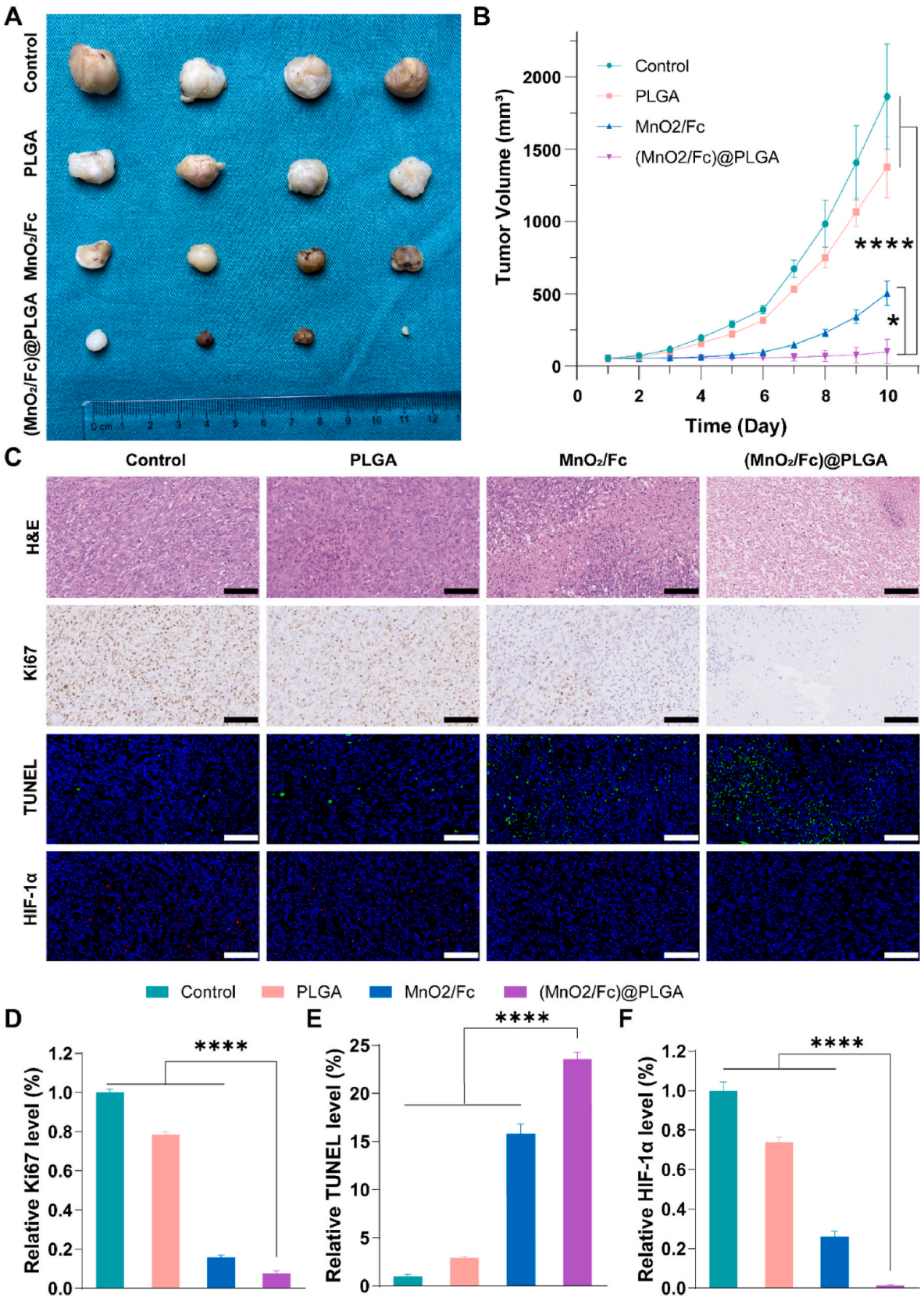

Fig. 5. Anti-tumor effects of (MnO_2/Fc)@PLGA hydrogel in vivo. (A) Images of MNNG/HOS tumors were removed on the 10th day after different treatments. (B) The change curves of tumor volume after corresponding treatments. The staining of (C) H&E, (D) Ki67, (E) TUNEL, and (F) HIF-1α of tumor slices collected from MNNG/HOS tumor-bearing nude mice after different treatments (scale bar: 100 μm, ****$p < 0.0001$).

B, when compared to the control and PLGA groups, the (MnO_2/Fc)@PLGA group could significantly inhibit tumor growth. However, the MnO_2/Fc group showed good tumor inhibition at the beginning of the experiment, but 6 days later, the tumor started to grow rapidly. This indicated that (MnO_2/Fc)@PLGA could continuously inhibit tumor growth compared with MnO_2/Fc alone. As previously mentioned, for nanoparticles delivery in the nanoparticle-loaded hydrogel, the hydrogel system acts as a supply station that can retain the loaded therapeutic nanoparticles around the tumor, thus maintaining the concentration of the nanoparticles at sufficient therapeutic levels.

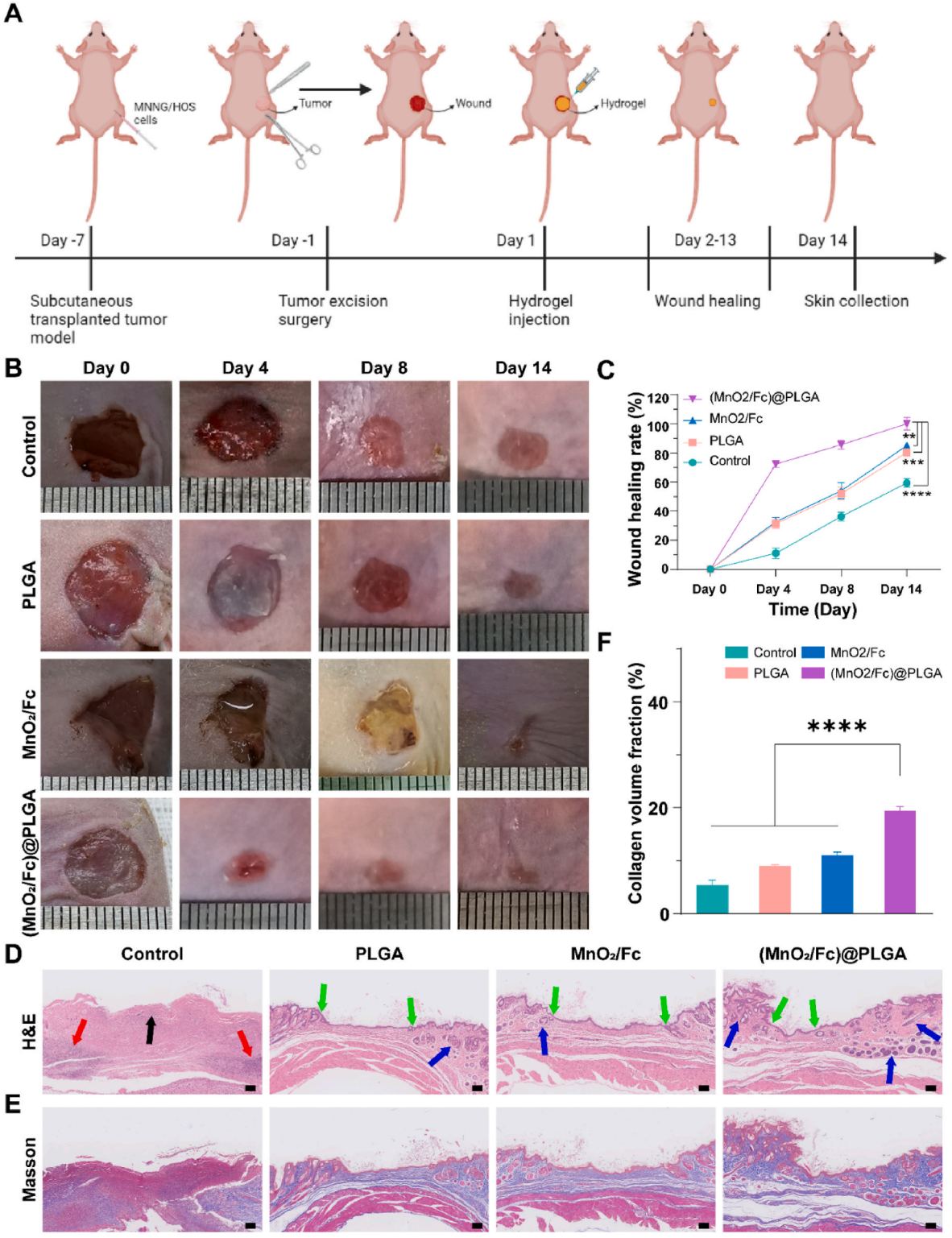

Fig. 6. (MnO_2/Fc)@PLGA hydrogel promotes wound healing in vivo. (A) Schematic diagram of postoperative trauma model of osteosarcoma and wound healing with (MnO_2/Fc)@PLGA. (B) Images of the wound healing process treated with PBS, PLGA, MnO_2, and (MnO_2/Fc)@PLGA. (C) The wound healing rates of the four groups at different times in vivo. (D) H&E staining of the skin slices was excised on day 14. (E, F) Masson staining of the skin slices was excised on day 14 (black arrow: scab, red arrow: inflammatory infiltration, green arrow: epithelial tissue, blue arrow: glands and hair follicles; scale bar: 100 μm, ****$p < 0.0001$).

The H&E staining, Ki67 staining, and TUNEL fluorescence staining of the excised tumors for histological analysis were conducted. The proliferation of tumor cells was evaluated by immunohistochemical Ki67 staining, and the expression of Ki67 in tumor cells in the (MnO_2/Fc)@PLGA hydrogel group was decreased (Fig. 5C and D), indicating that the proliferation ability of tumor cells was dramatically decreased after treatment. Apoptosis was analyzed by TUNEL fluorescence staining, and the green fluorescence of the (MnO_2/Fc)@PLGA hydrogel group was noticeably stronger than that of the other groups, demonstrating the potent anti-tumor properties of (MnO_2/Fc)@PLGA hydrogel (Fig. 5C and E). Additionally, to investigate the ability of (MnO_2/Fc)@PLGA hydrogel to improve tumor hypoxic microenvironment, the level of HIF-1α was further detected. The significantly decreased expression of HIF-1α was observed in the (MnO_2/Fc)@PLGA hydrogel group, indicating that tumor hypoxia was improved (Fig. 5C and F). Accordingly, (MnO_2/Fc)@PLGA hydrogel has a potent anti-osteosarcoma potential due to it can constantly release MnO_2/Fc at the tumor site, enhancing the efficacy of CDT and improving the tumor hypoxic microenvironment.

2.5. *(MnO₂/Fc)@PLGA hydrogel promotes surgical wound healing in vivo*

At present, surgery is still important in the treatment of osteosarcoma, but local recurrence and wound healing after surgery have yet to be addressed. Therefore, we further tested the anti-tumor recurrence and wound healing ability of (MnO_2/Fc)@PLGA hydrogel in vivo. Firstly, the postoperative trauma model of osteosarcoma was established. As shown in Fig. 6A, the subcutaneous xenograft tumor model was first constructed by subcutaneous injection of MNNG/HOS cells into nude mice, and the postoperative trauma model was constructed by tumor resection 7 days later. Then, an appropriate amount of (MnO_2/Fc)@PLGA hydrogel was applied to the wound to observe the wound healing. As shown in Fig. 6B and C, the (MnO_2/Fc)@PLGA hydrogel group showed significantly better wound contraction than the control, PLGA, and MnO_2/Fc groups. And at 4, 8, and 14 days, the (MnO_2/Fc)@PLGA hydrogel treatment group had the lowest wound of all the groups. Additionally, to monitor the healing of subcutaneous fibrous tissue, the skin slices excised on day 14 were stained with H&E and Masson. The H&E staining results revealed that the (MnO_2/Fc)@PLGA group had a thicker epidermis (green arrow) and more skin appendages, such as more glands and hair follicles (blue arrow) (Fig. 6D). Furthermore, the Masson staining of skin slices exhibited a significant increase in the subcutaneous collagen fibers after the treatment of (MnO_2/Fc)@PLGA hydrogel (Fig. 6E and F). At the same time, the wound healing capacity of the PLGA and MnO_2/Fc groups was also better than the control group. The reason may be that PLGA could better adhesion and seal wound to promote wound healing, and MnO_2/Fc could promote H_2O_2 decomposition to produce O_2, efficiently alleviate hypoxia, and promote fibroblast proliferation.

Besides, angiogenesis is also essential for wound healing. Therefore, we examined the expression of angiogenic factors within the treated skin sections. The angiogenesis was detected by immunofluorescence double staining with CD31 and α-SMA, and double staining with HIF-1α and VEGFA. As shown in Fig. 7A–C, the CD31 and α-SMA expression were significantly increased after treatment of (MnO_2/Fc)@PLGA hydrogel. Additionally, HIF-1α and VEGFA expression also increased significantly in the (MnO_2/Fc)@PLGA hydrogel group (Fig. 7D–F). Therefore, after the treatment of (MnO_2/Fc)@PLGA hydrogel, more angiogenic factors increased in the skin, which further promoted wound healing.

3. Conclusions

In fact, there are a lot of benefits to using hydrogels containing nanoparticles in avoiding tumor recurrence following excision surgery. Firstly, the local and sustained nanoparticles delivery system enhances the therapeutic efficacy by allowing the nanoparticles to accumulate precisely at the surgical site, ensuring prolonged exposure to the tumor bed while minimizing systemic toxic side effects. Secondly, the hydrogel matrix improves the permeability of the therapeutic agents, facilitating better penetration into the surrounding tissues, which is crucial for targeting residual tumor cells that may not be fully resected. Thirdly, the nanoparticles embedded in the hydrogel have unique properties that augment the therapeutic effect, such as promoting ROS generation in CDT, which selectively kills tumor cells. Lastly, the hydrogel itself forms a protective barrier over the wound, not only isolating residual tumor cells but also providing a favorable environment for wound healing by gradually releasing therapeutic ions like Mn^{2+}/Fe^{2+} and maintaining a moist wound interface. These features collectively make the nanoparticle-laden hydrogels an effective strategy for both promoting post-surgical recovery and preventing osteosarcoma recurrence.

In this study, we developed an injectable hydrogel-based therapeutic platform for simultaneous anti-tumor recurrence and wound healing after osteosarcoma surgery (Fig. 8). By local injection of (MnO_2/Fc)@PLGA hydrogel into the surgical wound, MnO_2/Fc could catalyze endogenous H_2O_2 to create O_2, alleviate the hypoxic microenvironment, and prevent the local recurrence of osteosarcoma. Additionally, (MnO_2/Fc)@PLGA hydrogel could promote angiogenesis and subcutaneous fibrous tissue proliferation, which was beneficial for surgical wound healing. Collectively, (MnO_2/Fc)@PLGA hydrogel could inhibit local recurrence of osteosarcoma through CDT, eliminate the adverse effects of H_2O_2, and promote wound healing, thereby providing a novel strategy for tumor therapy and wound healing.

4. Materials and methods

4.1. *Materials*

PLGA-PEG-PLGA triblock copolymer was purchased from Ruixibio LTD (Xi'an, China). MnO_2 nanoparticles were bought from XFNANO (Nanjing, China). Ferrocenecarboxylic acid was acquired from Ruixibio LTD (Xi'an, China). Sigma-Aldrich (USA) offered hematoxylin and eosin (H&E). Invitrogen (USA) provided the calcein-AM/propidium iodide (PI) and 4′,6-diamidino-2-phenylindole (DAPI) chemicals. Solarbio (Beijing, China) provided the ROS detection kit (2′,7′-dichlorofluorescein diacetate, DCFH-DA). The following items were purchased from Gibco LifeTechnologies (USA): Dulbecco's modified eagle medium (DMEM), F12 media, fetal bovine serum (FBS), penicillin-streptomycin, phosphate buffer solution (PBS), and trypsin-EDTA. Solarbio LTD (Beijing, China) provided the 0.1 % crystal violet staining solution. Cell Counting Kit-8 (CCK-8) was bought from Dojindo Laboratories Co. LTD (Kumamoto, Japan). Hydrogen peroxide (H_2O_2, 30 wt%) was provided by Sino pharm Chemical Reagent Co.

4.2. *Synthesis of PLGA-PEG-PLGA triblock copolymer, MnO_2 nanoparticles and MnO_2/Fc NPs solution*

PLGA-PEG-PLGA triblock copolymer was produced by ring-opening polymerization of lactide (LA) and glycolide (GA) in a 2:1 M ratio with PEG serving as an initiator and $Sn(Oct)_2$ functioning as a catalyst. Additionally, ethylene glycol and potassium permanganate ($KMnO_4$) were used to create manganese dioxide (MnO_2) nanoparticles. Specially, we dissolved 6.94 g of $KMnO_4$ in 400 mL of sterile double-steamed water. A slow addition of 10 mL of ethylene glycol was made while stirring continuously. The mixture was then subjected to ultrasonic dispersion for 2 h to ensure uniformity. Following this, the solution was centrifuged, and the precipitate was washed with deionized water and then with absolute ethanol three times to remove any unreacted materials and impurities. Finally, the washed particles were dried and ground to obtain MnO_2 nanoparticles.

For the preparation of MnO_2/Fc nanoparticles, 10 mg of the synthesized MnO_2 nanoparticles and 10 mg ferrocene (Fc) nanoparticles were combined in 10 mL of sterile double-steamed water. The mixture

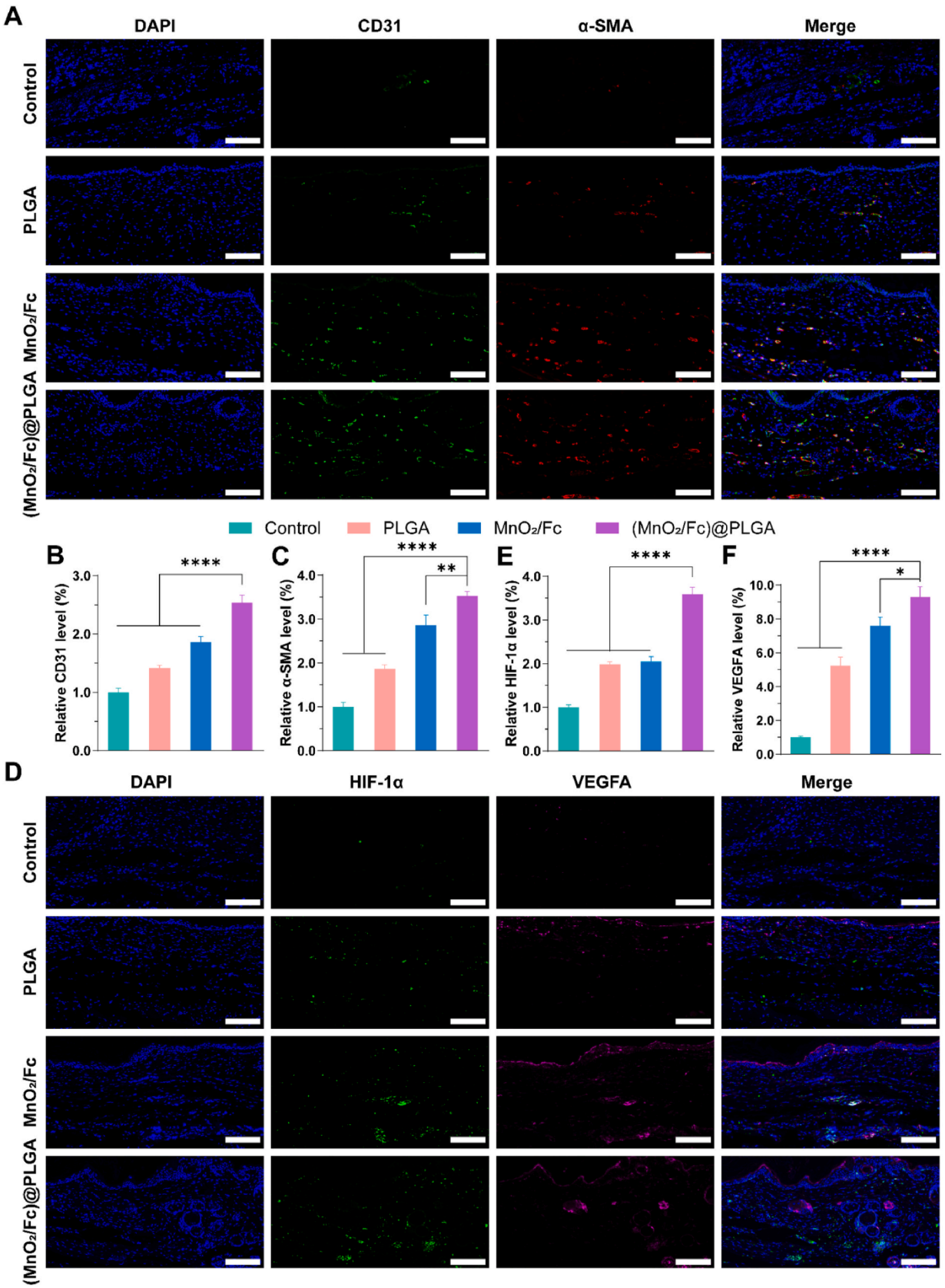

Fig. 7. (MnO_2/Fc)@PLGA hydrogel enhances angiogenesis in vivo. (A, B, C) Immunofluorescence double staining of CD31 and α-SMA of the skin slices after different treatments. (D, E, F) Immunofluorescence double staining of HIF-1α and VEGFA of the skin slices after different treatments (scale bar: 100 μm, ****$p < 0.0001$).

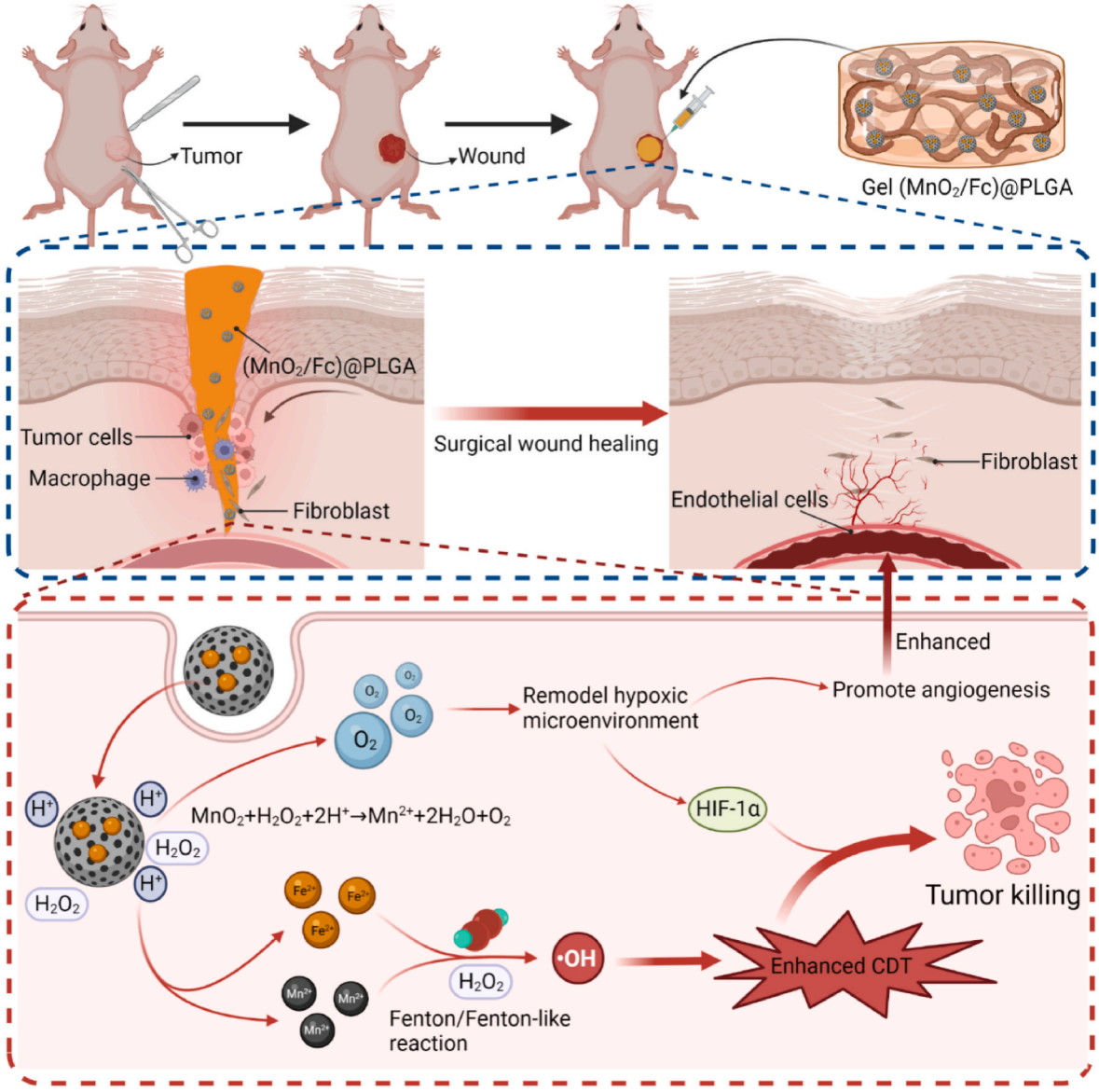

Fig. 8. An injectable hydrogel-based therapeutic platform (MnO_2/Fc)@PLGA was constructed for simultaneous anti-tumor recurrence and wound healing after osteosarcoma surgery. By local injection into the surgical wound, (MnO_2/Fc)@PLGA hydrogel could inhibit local recurrence of osteosarcoma through CDT, eliminate the adverse effects of H_2O_2, alleviate the hypoxic microenvironment, and promote wound healing, thereby providing a novel strategy for tumor therapy and wound healing.

was stirred thoroughly to achieve a uniform dispersion, resulting in a 1 mg/mL MnO_2/Fc nanoparticles solution.

4.3. Synthesis of (MnO_2/Fc)@PLGA hydrogel

Temperature-sensitive hydrogel solution was created by mixing and stirring the right quantity of synthetic copolymer PLGA and sterile double-steamed water (20 wt%: 0.1 g PLGA added to 400 μL water; 25 wt%: 0.1 g PLGA added to 300 μL water; 30 wt%: 0.3 g PLGA added to 700 μL water). Then the created thermosensitive hydrogel solution (25 wt% PLGA hydrogel) was combined with the required amount of MnO_2 nanoparticles and Fc (1 mg/mL (MnO_2/Fc)@PLGA hydrogel: 1 mg MnO_2 and 1 mg Fc added to 1 mL 25 wt% PLGA hydrogel), swirled at low temperature until fully combined, and then left at 4 °C overnight to make the (MnO_2/Fc)@PLGA nanoparticle-loaded hydrogel solution. By either injecting the solution into animals or incubating the solution at 37 °C, the (MnO_2/Fc)@PLGA hydrogel was created.

4.4. Characterization of PLGA, MnO_2/Fc, and (MnO_2/Fc)@PLGA

Hydrogel samples were lyophilized after being quickly frozen in liquid nitrogen. The morphology of the prepared hydrogels and nanoparticles was examined by scanning electron microscopy (SEM) (Hitachi Regulus 8230). EDS (Quanta FEG 250) was used to test the element distribution. On a Thermo Fisher Nicolet 6700 FTIR spectrometer, Fourier transforms infrared spectra (FTIR) were scanned in the 500-4000 cm^{-1} range. By using ^1H NMR, the chemical structure of the synthesized PLGA was confirmed. A Bruker AV 300 NMR spectrometer was used to record this characterization. In this test, $CDCl_3$ served as the standard solvent. The dynamic rheological behavior of hydrogel with the increase in temperature was measured by a rotating rheometer (Anton Paar, Graz, Austria), and the energy storage modulus and loss modulus of hydrogel was obtained. The hydrogel solution was placed on the detection plate, the parallel diameter of detection was 8 mm, the initial temperature of detection was 10 °C, the temperature was increased at 0.5 °C per minute until it rose to 70 °C, the measured strain

amplitude parameter was 1 %, and the angular frequency parameter was set as 1 rad/s. In addition, the sol-to-gel transition temperature of PLGA and (MnO_2/Fc)@PLGA solution was determined by tube inversion method. Prepared PLGA and (MnO_2/Fc)@PLGA solutions of different concentrations, take 0.5 mL of these solutions and add them to the corresponding vials with a diameter of 16 mm, and place these vials in a water bath. The measured temperature range was 10–60 °C, and the temperature rise interval was 1 °C, and the vial was inverted after constant temperature for 10 min at each temperature to observe whether the solution flowed within 30 s. If it did not flow, it was considered that gel transition occurred, and the temperature was the sol-to-gel transition temperature.

4.5. *In vitro* nanoparticles release from hydrogel

The (MnO_2/Fc)@PLGA solutions with a loading concentration of 1 mg/mL were prepared according to the previous method, and 0.5 mL of the solutions were added into the corresponding vials with a diameter of 16 mm. The solution was transformed into gel after being placed at 37 °C for 10 min. Then, 3 mL PBS buffer was slowly added to each vial and placed in a constant temperature water bath shaker at 37 °C. The 2 mL PBS buffer was taken out at the specified time interval and stored at low temperature away from light for detection together, and the same amount of new PBS buffer was added. The contents of MnO_2 and Fc in the buffer were detected by inductively coupled plasma mass spectrometry (ICP-MS; Xseriesll, Thermo Scientific).

4.6. *In vitro generation of O_2*

In a sealed chamber coupled with an oxygen electrode (Dissolved Oxygen Meter, AZ-8402, Guangdong, China) at 37 °C, disperse MnO_2/Fc (Mn, 200 μM) in PBS with different pH (7.4 and 6.5), blow with N_2 for 30 min to remove dissolved O_2, and then inject H_2O_2 solution (100 μM), measure the generated O_2 through the oxygen electrode.

4.7. *Degradation of PLGA in vitro*

0.5 mL prepared 25 wt% PLGA solution was added into a vial with a diameter of 16 mm, and the solution was transformed into gel after being placed at 37 °C for 10 min. After weighing the gel, 3 mL PBS buffer was slowly added into the vial, and place the vial in a constant temperature water bath shaker (50 shakes/min) at 37 °C. Removed PBS buffer solution within the specified time intervals, weighted the gel, and added new PBS buffer solution.

4.8. *Degradation and histocompatibility of PLGA in vivo*

Beijing Huafukang Bioscience Co. INC. furnished the male Balb/c nude mice (4–5 weeks). The Care and Use of Laboratory Animals of the National Institutes of Health provided oversight for all animal research, and the Committee on the Ethics of Animal Experiments of Huazhong University of Science and Technology gave its permission. A syringe was used to inject 200 μL 25 wt% PLGA solution into the subcutaneous of nude mice, and then the nude mice were euthanized at the set time (30 min, 7 d, 14 d and 21 d), and the skin at the injection site was cut open to observe the degradation of the gel in vivo. Simultaneously, the skin was sectioned and staining with H&E to observe the histological changes.

4.9. *Cell viability assay*

The MNNG/HOS cell line was acquired from Procell Life Science and Technology Co, LTD (Wuhan, China). All the cells were incubated at 37 °C under a 5 % CO_2 atmosphere. MNNG/HOS cells (5000 cells per well) were seeded in a 96-well plate for in vitro treatment and incubated for 24 h. The following four cell group tasks were then carried out: control, PLGA, MnO_2/Fc, and (MnO_2/Fc)@PLGA groups. The medicines ranged in concentration from 0.00390625 g/L to 0.5 g/L. After 24 h of material incubation, the culture medium was changed to 100 μl of fresh media containing 10 % CCK-8 solution, which was then incubated at 37 °C in the dark for 1, 2, and 4 h. A microplate reader measured the supernatant's absorbance at 450 nm for each well. Additionally, four sets (concentration of 0.03 g/L) of cells were exposed for intervals of 24, 48, and 72 h before the 10 % CCK-8 solution was replenished and the absorbance was determined as described before.

4.10. *Live-dead staining assay*

24-well plates containing tumor cells (10^4 cells per well) were planted, incubated for 24 h, then co-cultured with various materials (PBS, 25 wt% PLGA, MnO_2/Fc, (MnO_2/Fc)@PLGA, concentration of 0.03 g/L) for 12 h. In accordance with the product's instructions, Calcein-AM and PI were then employed to stain the cells. A fluorescent microscope was used to view both the living and dead cells.

4.11. *Cell proliferation and migration assays*

To test the ability of cells to proliferate, 1000 cells per well were seeded into 6-well plates, which were then cultivated for 10 days in 10 % FBS medium with medium changes every 3 days. On day 10, cells were fixed with 4 % paraformaldehyde for 15 min, and then stained for 30 min with 0.1 % crystal violet. In order to conduct the Transwell assay, 2 $\times$ 10^4 cells were seeded into the top chamber of transwell chamber plates (24-well format, 8 m pore size, BD Biosciences, St. Louis, MO) using 100 μl of serum-free DMEM. The growth media that included 20 % FBS was poured into the bottom well. Cells were cultured for 24 h before being fixed for 15 min with 4 % paraformaldehyde and stained for 30 min with 0.1 % crystal violet. The average number of migrating cells was then determined using a light microscope.

4.12. *Detection of ROS level in vitro*

Prior to being washed three times with PBS, MNNG/HOS cells were initially treated with various substances (PBS, PLGA, MnO_2/Fc, and (MnO_2/Fc)@PLGA, concentration of 0.03 g/L) for 4 h in 5 % CO_2 at 37 °C. Afterward, tagged cells for 20 min with a DCFH-DA probe to gauge the degree of ROS generation, and then observed and captured images of the cells using a fluorescence microscope (Olympus Corporation, Tokyo, Japan).

4.13. *Subcutaneous xenograft tumor model*

Beijing Huafukang Bioscience Co. INC. furnished the male Balb/c nude mice (4–5 weeks). The Care and Use of Laboratory Animals of the National Institutes of Health provided oversight for all animal research, and the Committee on the Ethics of Animal Experiments of Huazhong University of Science and Technology gave its permission ([2022] IACUC Number: 3069). In a nutshell, $5x10^6$ MNNG/HOS cells were subcutaneously implanted to create MNNG/HOS tumor-bearing animals. The following formula was used to determine the tumor volume: Volume(mm^3) = $ab^2/2$ (a: the length of tumor, b: the width of tumor).

4.14. *Anti-tumor efficacy and systemic toxicity evaluation in vivo*

The MNNG/HOS tumor-bearing mice were divided into four groups (n = 4 for each group) randomly: control, PLGA, MnO_2/Fc, and (MnO_2/Fc)@PLGA groups. When the tumor volume reached 50 mm^3, 100 μL of PBS, PLGA, MnO_2/Fc, or (MnO_2/Fc)@PLGA, with a concentration of 0.5 g/L was injected adjacent to the tumor, only once. Nude mice's body weight and tumor volume were assessed every day while they were receiving therapy. The mice were euthanized on the 10th day, and the tumors and important organs were harvested. Hematoxylin-eosin (H&E) staining was used to examine the major organs in order to assess the

systemic toxicity and biocompatibility. To investigate the mechanism of (MnO_2/Fc)@PLGA hydrogel's anti-tumor effects, H&E and Ki67 staining, TUNEL and HIF-1α immunofluorescence staining were done on tumor tissue slices.

4.15. Postoperative trauma model and the effects of wound healing in vivo

The subcutaneous xenograft tumor model was first constructed according to the previous method *4.13*, and the tumor was resected 7 days later to construct the postoperative trauma model [37]. The postoperative trauma mice were divided into four groups (n = 4 for each group) randomly: control, PLGA, MnO_2/Fc, and (MnO_2/Fc)@PLGA groups. After the treatment of 100 μL PBS, PLGA, MnO_2/Fc, or (MnO_2/Fc)@PLGA, with a concentration of 0.5 g/L, the wound was covered with gauze. The wound was photographed every 2 days. On the 14th day, the entire wound skin was excised and fixed, and the slices were stained with H&E and Masson. In addition, CD31, SMA, HIF-1α, and VEGFA immunofluorescence double staining to detect the mechanism of (MnO_2/Fc)@PLGA hydrogel to promote wound healing.

4.16. Statistical analysis

For the statistical analysis, GraphPad 9.0 was utilized as the software. The two-tailed student t-test was employed when there was a significant difference between two groups, and the one-way analysis of variance (ANOVA) was used when there were three or more groups. A result was considered statistically significant if its p-value was less than 0.05 (*$p < 0.05$, **$p < 0.01$, ***$p < 0.001$, ****$p < 0.0001$).

CRediT authorship contribution statement

Lutong Wang: Writing – original draft, Methodology, Investigation. **Haoyu Guo:** Writing – original draft, Methodology, Investigation. **Weiyue Zhang:** Writing – original draft, Supervision, Methodology, Investigation. **Xingyin Li:** Software, Investigation. **Ziliang Su:** Software, Investigation. **Xin Huang:** Writing – review & editing, Investigation, Funding acquisition.

Data sharing statement

The data that supports the findings of this study are available from the corresponding author upon reasonable request.

Funding

This study is supported by National Natural Science Foundation of China (82203059, 82300932) and Hubei Natural Science Foundation (2022CFB656).

Declaration of competing interest

No conflict of interest exits in the submission of this manuscript.

References

[1] J. Gill, R. Gorlick, Advancing therapy for osteosarcoma, Nat. Rev. Clin. Oncol. 18 (2021) 609–624, https://doi.org/10.1038/s41571-021-00519-8.
[2] R.L. Siegel, K.D. Miller, A. Jemal, Cancer statistics, CA A Cancer J. Clin. 68 (2018) 7–30, https://doi.org/10.3322/caac.21442, 2018.
[3] H.C. Beird, S.S. Bielack, A.M. Flanagan, J. Gill, D. Heymann, K.A. Janeway, J. A. Livingston, R.D. Roberts, S.J. Strauss, R. Gorlick, Osteosarcoma, Nat Rev Dis Primers 8 (2022) 77, https://doi.org/10.1038/s41572-022-00409-y.
[4] C. Chen, L. Xie, T. Ren, Y. Huang, J. Xu, W. Guo, Immunotherapy for osteosarcoma: fundamental mechanism, rationale, and recent breakthroughs, Cancer Lett. 500 (2021) 1–10, https://doi.org/10.1016/j.canlet.2020.12.024.
[5] X. Huang, L. Wang, H. Guo, W. Zhang, Z. Shao, Single-cell transcriptomics reveals the regulative roles of cancer associated fibroblasts in tumor immune microenvironment of recurrent osteosarcoma, Theranostics 12 (2022) 5877–5887, https://doi.org/10.7150/thno.73714.
[6] J.S. Whelan, L.E. Davis, Osteosarcoma, chondrosarcoma, and chordoma, J. Clin. Orthod. 36 (2018) 188–193, https://doi.org/10.1200/JCO.2017.75.1743.
[7] X. Huang, J. Chen, W. Wu, W. Yang, B. Zhong, X. Qing, Z. Shao, Delivery of MutT homolog 1 inhibitor by functionalized graphene oxide nanoparticles for enhanced chemo-photodynamic therapy triggers cell death in osteosarcoma, Acta Biomater. 109 (2020) 229–243, https://doi.org/10.1016/j.actbio.2020.04.009.
[8] B. Zhang, Y. Zhang, R. Li, J. Li, X. Lu, Y. Zhang, The efficacy and safety comparison of first-line chemotherapeutic agents (high-dose methotrexate, doxorubicin, cisplatin, and ifosfamide) for osteosarcoma: a network meta-analysis, J. Orthop. Surg. Res. 15 (2020) 51, https://doi.org/10.1186/s13018-020-1576-0.
[9] Y. Wang, D. Wang, Y. Zhang, H. Xu, L. Shen, J. Cheng, X. Xu, H. Tan, X. Chen, J. Li, Tumor microenvironment-adaptive nanoplatform synergistically enhances cascaded chemodynamic therapy, Bioact. Mater. 22 (2023) 239–253, https://doi.org/10.1016/j.bioactmat.2022.09.025.
[10] Z. Tang, Y. Liu, M. He, W. Bu, Chemodynamic therapy: tumour microenvironment-mediated Fenton and fenton-like reactions, Angew. Chem. Int. Ed. 58 (2019) 946–956, https://doi.org/10.1002/anie.201805664.
[11] C. Jia, Y. Guo, F.-G. Wu, Chemodynamic therapy via Fenton and fenton-like nanomaterials: strategies and recent advances, Small 18 (2022) 2103868, https://doi.org/10.1002/smll.202103868.
[12] W. Feng, X. Han, R. Wang, X. Gao, P. Hu, W. Yue, Y. Chen, J. Shi, Nanocatalysts-augmented and photothermal-enhanced tumor-specific sequential nanocatalytic therapy in both NIR-I and NIR-II biowindows, Adv. Mater. 31 (2019) 1805919, https://doi.org/10.1002/adma.201805919.
[13] T. He, Y. Yuan, C. Jiang, N.T. Blum, J. He, P. Huang, J. Lin, Light-triggered transformable ferrous ion delivery system for photothermal primed chemodynamic therapy, Angew. Chem. Int. Ed. 60 (2021) 6047–6054, https://doi.org/10.1002/anie.202015379.
[14] W.A. Wlassoff, C.D. Albright, M.S. Sivashinski, A. Ivanova, J.G. Appelbaum, R. I. Salganik, Hydrogen peroxide overproduced in breast cancer cells can serve as an anticancer prodrug generating apoptosis-stimulating hydroxyl radicals under the effect of tamoxifen-ferrocene conjugate, J. Pharm. Pharmacol. 59 (2007) 1549–1553, https://doi.org/10.1211/jpp.59.11.0013.
[15] W.-J. Wang, Y.-Y. Ling, Y.-M. Zhong, Z.-Y. Li, C.-P. Tan, Z.-W. Mao, Ferroptosis-enhanced cancer immunity by a ferrocene-appended iridium(III) diphosphine complex, Angew. Chem. Int. Ed. 61 (2022) e202115247, https://doi.org/10.1002/anie.202115247.
[16] Y. Wang, S. Zhang, J. Wang, Q. Zhou, J.F. Mukerabigwi, W. Ke, N. Lu, Z. Ge, Ferrocene-containing polymersome nanoreactors for synergistically amplified tumor-specific chemodynamic therapy, J. Contr. Release 333 (2021) 500–510, https://doi.org/10.1016/j.jconrel.2021.04.007.
[17] S.Y. Lee, J. Park, D.I. Jeong, C. Hwang, J. Lee, K. Lee, H.-J. Kim, H.-J. Cho, Ferrocene and glucose oxidase-installed multifunctional hydrogel reactors for local cancer therapy, J. Contr. Release 349 (2022) 617–633, https://doi.org/10.1016/j.jconrel.2022.07.017.
[18] Y. Hu, S. Mignani, J.-P. Majoral, M. Shen, X. Shi, Construction of iron oxide nanoparticle-based hybrid platforms for tumor imaging and therapy, Chem. Soc. Rev. 47 (2018) 1874–1900, https://doi.org/10.1039/C7CS00657H.
[19] D.R. van Staveren, N. Metzler-Nolte, Bioorganometallic chemistry of ferrocene, Chem. Rev. 104 (2004) 5931–5986, https://doi.org/10.1021/cr0101510.
[20] W. Li, X. Zhou, S. Liu, J. Zhou, H. Ding, S. Gai, R. Li, L. Zhong, H. Jiang, P. Yang, Biodegradable nanocatalyst with self-supplying fenton-like ions and H2O2 for catalytic cascade-amplified tumor therapy, ACS Appl. Mater. Interfaces 13 (2021) 50760–50773, https://doi.org/10.1021/acsami.1c14598.
[21] D. Zhu, X.-H. Zhu, S.-Z. Ren, Y.-D. Lu, H.-L. Zhu, Manganese dioxide (MnO2) based nanomaterials for cancer therapies and theranostics, J. Drug Target. 29 (2021) 911–924, https://doi.org/10.1080/1061186X.2020.1815209.
[22] T. Lin, X. Zhao, S. Zhao, H. Yu, W. Cao, W. Chen, H. Wei, H. Guo, O_2-generating MnO_2 nanoparticles for enhanced photodynamic therapy of bladder cancer by ameliorating hypoxia, Theranostics 8 (2018) 990–1004, https://doi.org/10.7150/thno.22465.
[23] X. Huang, W. Zhang, Overcoming T cell exhaustion in tumor microenvironment via immune checkpoint modulation with nano-delivery systems for enhanced immunotherapy, Small Methods 8 (2024) 2301326, https://doi.org/10.1002/smtd.202301326.
[24] S. Guan, X. Liu, C. Li, X. Wang, D. Cao, J. Wang, L. Lin, J. Lu, G. Deng, J. Hu, Intracellular mutual amplification of oxidative stress and inhibition multidrug resistance for enhanced sonodynamic/chemodynamic/chemo therapy, Small 18 (2022) 2107160, https://doi.org/10.1002/smll.202107160.
[25] Y. Zhao, Y. Pan, K. Zou, Z. Lan, G. Cheng, Q. Mai, H. Cui, Q. Meng, T. Chen, L. Rao, L. Ma, G. Yu, Biomimetic manganese-based theranostic nanoplatform for cancer multimodal imaging and twofold immunotherapy, Bioact. Mater. 19 (2023) 237–250, https://doi.org/10.1016/j.bioactmat.2022.04.011.
[26] T. Xiao, M. He, F. Xu, Y. Fan, B. Jia, M. Shen, H. Wang, X. Shi, Macrophage membrane-camouflaged responsive polymer nanogels enable magnetic resonance imaging-guided chemotherapy/chemodynamic therapy of orthotopic glioma, ACS Nano 15 (2021) 20377–20390, https://doi.org/10.1021/acsnano.1c08689.
[27] S. Cheng, Y. Shi, C. Su, Y. Li, X. Zhang, MnO2 nanosheet-mediated generalist probe: cancer-targeted dual-microRNAs detection and enhanced CDT/PDT synergistic therapy, Biosens. Bioelectron. 214 (2022) 114550, https://doi.org/10.1016/j.bios.2022.114550.
[28] S. Bochani, A. Zarepour, A. Kalantari-Hesari, F. Haghi, M.-A. Shahbazi, A. Zarrabi, S. Taheri, A. Maleki, Injectable, antibacterial, and oxygen-releasing chitosan-based

hydrogel for multimodal healing of bacteria-infected wounds, J. Mater. Chem. B 11 (2023) 8056–8068, https://doi.org/10.1039/D3TB01278F.
[29] Y. Guo, X. Zheng, T. Gai, Z. Wei, S. Zhang, Co-biomembrane-coated Fe3O4/MnO2 multifunctional nanoparticles for targeted delivery and enhanced chemodynamic/photothermal/chemo therapy, Chem. Commun. 57 (2021) 5754–5757, https://doi.org/10.1039/D1CC01375K.
[30] J. Xiao, G. Zhang, R. Xu, H. Chen, H. Wang, G. Tian, B. Wang, C. Yang, G. Bai, Z. Zhang, H. Yang, K. Zhong, D. Zou, Z. Wu, A pH-responsive platform combining chemodynamic therapy with limotherapy for simultaneous bioimaging and synergistic cancer therapy, Biomaterials 216 (2019) 119254, https://doi.org/10.1016/j.biomaterials.2019.119254.
[31] L.-L. Bu, J. Yan, Z. Wang, H. Ruan, Q. Chen, V. Gunadhi, R.B. Bell, Z. Gu, Advances in drug delivery for post-surgical cancer treatment, Biomaterials 219 (2019) 119182, https://doi.org/10.1016/j.biomaterials.2019.04.027.
[32] H. Liu, X. Shi, D. Wu, F. Kahsay Khshen, L. Deng, A. Dong, W. Wang, J. Zhang, Injectable, biodegradable, thermosensitive nanoparticles-aggregated hydrogel with tumor-specific targeting, penetration, and release for efficient postsurgical prevention of tumor recurrence, ACS Appl. Mater. Interfaces 11 (2019) 19700–19711, https://doi.org/10.1021/acsami.9b01987.
[33] X. Huang, L. Wang, H. Guo, W. Zhang, Macrophage membrane-coated nanovesicles for dual-targeted drug delivery to inhibit tumor and induce macrophage polarization, Bioact. Mater. 23 (2023) 69–79, https://doi.org/10.1016/j.bioactmat.2022.09.027.
[34] Z. Wang, B. Ding, Y. Zhao, Y. Han, Y. Sheng, L. Tao, X. Shen, J. Zhou, L. Jiang, Y. Ding, Tumor-oriented mathematical models in hydrogel regulation for precise topical administration regimens, J. Contr. Release 345 (2022) 610–624, https://doi.org/10.1016/j.jconrel.2022.03.042.
[35] W. Zhang, X. Yang, X. Huang, L. Chen, Bioinspired nanovesicles released from injectable hydrogels facilitate diabetic wound healing by regulating macrophage polarization and endothelial cell dysfunction, J. Nanobiotechnol. 21 (2023) 358, https://doi.org/10.1186/s12951-023-02119-3.
[36] Q. Yao, Q.-H. Lan, X. Jiang, C.-C. Du, Y.-Y. Zhai, X. Shen, H.-L. Xu, J. Xiao, L. Kou, Y.-Z. Zhao, Bioinspired biliverdin/silk fibroin hydrogel for antiglioma photothermal therapy and wound healing, Theranostics 10 (2020) 11719–11736, https://doi.org/10.7150/thno.47682.
[37] M. Wang, S. Wang, Y. Pan, R. Yu, Z.-R. Zhang, Y. Fu, In situ gel implant for postsurgical wound management and extended chemoimmunotherapy against breast cancer recurrence, Acta Biomater. 138 (2022) 168–181, https://doi.org/10.1016/j.actbio.2021.10.039.
[38] Z. Jing, R. Ni, J. Wang, X. Lin, D. Fan, Q. Wei, T. Zhang, Y. Zheng, H. Cai, Z. Liu, Practical strategy to construct anti-osteosarcoma bone substitutes by loading cisplatin into 3D-printed titanium alloy implants using a thermosensitive hydrogel, Bioact. Mater. 6 (2021) 4542–4557, https://doi.org/10.1016/j.bioactmat.2021.05.007.
[39] H. Ma, C. He, Y. Cheng, D. Li, Y. Gong, J. Liu, H. Tian, X. Chen, PLK1shRNA and doxorubicin co-loaded thermosensitive PLGA-PEG-PLGA hydrogels for osteosarcoma treatment, Biomaterials 35 (2014) 8723–8734, https://doi.org/10.1016/j.biomaterials.2014.06.045.
[40] J. Chen, Y. Liu, G. Cheng, J. Guo, S. Du, J. Qiu, C. Wang, C. Li, X. Yang, T. Chen, Z. Chen, Tailored hydrogel delivering niobium carbide boosts ROS-scavenging and antimicrobial activities for diabetic wound healing, Small 18 (2022) 2201300, https://doi.org/10.1002/smll.202201300.
[41] J. Shi, L. Yu, J. Ding, PEG-based thermosensitive and biodegradable hydrogels, Acta Biomater. 128 (2021) 42–59, https://doi.org/10.1016/j.actbio.2021.04.009.
[42] Y. Xiong, L. Chen, P. Liu, T. Yu, C. Lin, C. Yan, Y. Hu, W. Zhou, Y. Sun, A.C. Panayi, F. Cao, H. Xue, L. Hu, Z. Lin, X. Xie, X. Xiao, Q. Feng, B. Mi, G. Liu, All-in-One: multifunctional hydrogel accelerates oxidative diabetic wound healing through timed-release of exosome and fibroblast growth factor, Small 18 (2022) 2104229, https://doi.org/10.1002/smll.202104229.
[43] Q. Wang, W. Qiu, M. Li, N. Li, X. Li, X. Qin, X. Wang, J. Yu, F. Li, L. Huang, D. Wu, Multifunctional hydrogel platform for biofilm scavenging and O2 generating with photothermal effect on diabetic chronic wound healing, J. Colloid Interface Sci. 617 (2022) 542–556, https://doi.org/10.1016/j.jcis.2022.03.040.
[44] W. Zhang, L. Wang, H. Guo, L. Chen, X. Huang, Dapagliflozin-loaded exosome mimetics facilitate diabetic wound healing by HIF-1α-Mediated enhancement of angiogenesis, Adv. Healthcare Mater. 12 (2023) 2202751, https://doi.org/10.1002/adhm.202202751.
[45] B. Yuan, Y. Zhang, Q. Wang, G. Ren, Y. Wang, S. Zhou, Q. Wang, C. Peng, X. Cheng, Thermosensitive vancomycin@PLGA-PEG-PLGA/HA hydrogel as an all-in-one treatment for osteomyelitis, Int. J. Pharm. 627 (2022) 122225, https://doi.org/10.1016/j.ijpharm.2022.122225.
[46] C. Jiao, N. Wei, D. Liu, J. Wang, S. Liu, F. Fu, T. Liu, T. Li, Sustainable Fenton-like degradation of methylene blue over MnO2-loaded poly(amidoxime-hydroxamic acid) cellulose microrods, Int. J. Biol. Macromol. 193 (2021) 1952–1961, https://doi.org/10.1016/j.ijbiomac.2021.11.026.
[47] Z. Song, R. Feng, M. Sun, C. Guo, Y. Gao, L. Li, G. Zhai, Curcumin-loaded PLGA-PEG-PLGA triblock copolymeric micelles: preparation, pharmacokinetics and distribution in vivo, J. Colloid Interface Sci. 354 (2011) 116–123, https://doi.org/10.1016/j.jcis.2010.10.024.
[48] S. Guo, Y. Ren, R. Chang, Y. He, D. Zhang, F. Guan, M. Yao, Injectable self-healing adhesive chitosan hydrogel with antioxidative, antibacterial, and hemostatic activities for rapid hemostasis and skin wound healing, ACS Appl. Mater. Interfaces 14 (2022) 34455–34469, https://doi.org/10.1021/acsami.2c08870.
[49] M. Zhang, Y. Chen, Q. Wang, C. Li, C. Yuan, J. Lu, Y. Luo, X. Liu, Nanocatalytic theranostics with intracellular mutual promotion for ferroptosis and chemo-photothermal therapy, J. Colloid Interface Sci. 657 (2024) 619–631, https://doi.org/10.1016/j.jcis.2023.12.006.